Title

The Cancer-Associated ATM R3008H Mutation Reveals the Link between ATM Activation and Its Exchange.

Journal

Cancer Research, 81(2)

Authors

Milanovic, Maja

Houghton, Lisa

Menolfi, Demis

et al.

Publication Date

2021-01-15

DOI

10.1158/0008-5472.CAN-20-2447

Peer reviewed

HHS Public Access

Author manuscript

Cancer Res. Author manuscript; available in PMC 2022 January 15.

Published in final edited form as:

Cancer Res. 2021 January 15; 81(2): 426–437. doi:10.1158/0008-5472.CAN-20-2447.

The cancer-associated ATM R3008H mutation reveals the link between ATM activation and its exchange

Maja Milanovic[1], **Lisa M. Houghton**[1,3], **Demis Menolfi**[1], **Ji-Hoon Lee**[4], **Kenta Yamamoto**[1,3], **Yang Li**[5], **Brian J. Lee**[1], **Jun Xu**[6], **Verna M. Estes**[1], **Dong Wang**[6], **Peter J. Mckinnon**[5], **Tanya T. Paull**[4], **Shan Zha**[1,2]

[1]Institute for Cancer Genetics, Department of Pathology and Cell Biology, College of Physicians and Surgeons, Columbia University, New York City, NY 10032

[2]Division of Pediatric Oncology, Hematology and Stem Cell Transplantation, Department of Pediatrics, College of Physicians & Surgeons, Columbia University, New York City, NY 10032

[3]Pathobiology and Human Disease Graduate Program, Department of Pathology and Cell Biology, Vagelos College for Physicians and Surgeons, Columbia University, New York, NY 10032

[4]Department of Molecular Biosciences, The University of Texas at Austin, Austin, TX 78712

[5]Department of Genetics, St. Jude Children's Research Hospital, Memphis, TN 38105

[6]Skaggs School of Pharmacy & Pharmaceutical Sciences, University of California San Diego, La Jolla, CA 92093

Abstract

ATM kinase is a tumor suppressor and a master regulator of the DNA damage response. Most cancer-associated alterations to ATM are missense mutations at the PI3-kinase regulatory domain (PRD) or the kinase domain. Expression of kinase-dead ATM protein solely accelerates lymphomagenesis beyond ATM loss. To understand how PRD suppresses lymphomagenesis, we introduced the cancer-associated PRD mutation-R3008H (R3016 in mouse) into mice. R3008H abrogated DNA damage- and oxidative stress-induced activation of ATM without consistently affecting ATM protein stability and recruitment. In contrast to the early embryonic lethality of $Atm^{KD/KD}$ mice, AtmR3016H ($Atm^{R/R}$) mice were viable, immunodeficient, and displayed spontaneous craniofacial abnormalities and delayed lymphomagenesis compared to $Atm^{-/-}$ controls. Mechanistically, R3008H rescued the tardy exchange of ATM-KD at DNA damage foci, indicating that PRD coordinates ATM activation with its exchange at DNA-breaks. Taken together, our results reveal a unique tumorigenesis profile for PRD mutations that is distinct from null or kinase-dead mutations.

Address Correspondence to Shan Zha at sz2296@columbia.edu.

Author contributions

KY and SZ generated the ATM-R3016H mouse models. MM, KY, LS, and DM analyzed lymphocyte development, lymphomagenesis, and DNA damage responses. BJL and VME assisted animal analyses. JL and TP performed the *in vitro* kinase analyses. BJL and MM performed live-cell imaging analyses. JX and DW provided the *in silico* model of the ATM kinase. YL and PJM performed the brain staining. MM and SZ wrote the manuscript.

The authors declare no conflict of interest.

Keywords

ATM; R3008H mutation; lymphomagenesis; neurological defects

Introduction

Ataxia-Telangiectasia (A-T) Mutated (ATM) is a master regulator of the DNA damage response (DDR) (1) and a tumor suppressor gene. Germline ATM inactivation causes A-T syndrome, characterized by cerebellar degeneration, immunodeficiency, and early-onset lymphomas. Over 90% of A-T patients have truncating or frameshift mutations with little or no ATM protein expression (2,3). Missense mutations of ATM are rare in A-T. Mouse models with complete loss of Atm (null) (4–8) recapitulate the immunodeficiency and lymphoma predisposition of A-T but do not develop overt neurological defects (9).

To ask whether ATM protein has a role in tumor suppression beyond its kinase activity, we and others generated mice expressing kinase-dead(KD) ATM. In contrast to the normal development of $Atm^{-/-}$ mice, $Atm^{KD/KD}$ and $Atm^{KD/-}$ mice died at embryonic day 9.5 with severe genomic instabilities (10,11), explaining the lack of missense mutations in live-born A-T patients. ATM ranks as the 3rd most common pathogenic germline variants in 10,389 adult cancers (12). Hematopoietic specific inactivation of the conditional allele in $Atm^{C/KD}$ mice causes earlier and more aggressive lymphomas than Atm deletion ($Atm^{C/-}$) (3,10). Notably, >70% of cancer-associated ATM alterations in The Cancer Genome Atlas (TCGA) are missense mutations that are highly enriched in the C-terminal kinase domain and the adjacent PI3-Kinase regulatory domain (PRD) (3). Notably, Neuron-specific expression of Atm-KD does not elicit Ataix in mice (13).

ATM suppresses lymphomagenesis by promoting DNA repair and activating cell-cycle checkpoints. ATM-deficient lymphocytes accumulate DNA double-strand breaks (DSB) during V(D)J recombination (14,15) and class switch recombination (CSR) (16–18). In the absence of checkpoints, the breaks participate in chromosomal translocations, leading to lymphomas in ~25% of A-T patients and nearly all Atm-null mice (1). Cells expressing Atm-KD display similar V(D)J recombination and CSR defects as of the $Atm^{-/-}$ cells (3,10). Both $Atm^{KD/-}$ and $Atm^{-/-}$ cells cannot phosphorylate Chk2 and p53, two checkpoint effectors (1).

How does Atm-KD cause embryonic lethality and accelerate tumors? $Atm^{KD/-}$ lymphocytes have more chromatid breaks than $Atm^{-/-}$ control and are hypersensitive to Topoisomerase I inhibitors, suggesting that Atm-KD impairs replication-associated DNA repair beyond the loss of ATM (3,10,11). $Atm^{KD/-}$, but not $Atm^{-/-}$ cells, show defects in the DR-GFP assay that measures homologous recombination (3,10,11). ATM is activated at the DNA damage sites by the MRE11-RAD50-NBS1 (MRN) complex. ATM Activation is concurrent with a dimer to monomer transition and inter-molecular auto-phosphorylation(1). ATM autophosphorylation at S1981 (corresponding to mouse S1987) are widely used as a marker for ATM activation (19,20). Transgenic mice carrying alanine substitution at one (Atm-S1987A) or two additional auto-phosphorylation sites were born alive with no detectable defects in ATM activation (21,22), suggesting auto-phosphorylation alone cannot explain the

severe genomic instabilities in $Atm^{KD/-}$ mice. In addition to DNA damage, reactive oxygen species (ROS) also activate ATM (23). But the physiological role of ROS induced ATM activation remains elusive.

The allosteric changes of PRD-I loop between Kα9 and Kα10 helices are implicated in the ATM and Tel1 activation (24–27) [Fig. 1A,1B, 1C and 1D]. Within PRD, C2991 is essential for ROS-induced ATM activation *in vitro* (23), and K3016 and S2996 are important for DNA damage-induced ATM acetylation and phosphorylation [Fig. 1B]. The R3008 (R3016 in mice) in the Kα10 helix is the most common cancer associated ATM missense mutation (3) [Fig. S1A and S1B]. To understand the impact of the PRD in ATM and its tumor suppressor functions, we generated the $Atm^{R/R}$ mice carrying R3016H mutation. Atm-R3016H protein is stable but cannot be efficiently activated by DNA damage or ROS. Yet, $Atm^{R/R}$ mice are viable and display spontaneous craniofacial defects and lymphoma spectrum that are distinct from both $Atm^{-/-}$ and $Atm^{KD/KD}$ mice (see Table S1). In cells, the R3008H mutation rescues the delayed exchange of ATM-KD at the DNA damage, suggesting R3008 allosterically coordinates ATM activation and exchange. With implications for A-T patients and ATM mutated cancers.

Materials and Methods

Mouse models and Generation of the $Atm^{R/R}$ mouse model

The $Atm^{-/-}$ mouse was described previously (28). The R3016H mutation (NP_031525.3) [Fig. 1A and 1B] and a silent Bgl II digestion site (no protein change) were embedded in the 3' arm and cloned into the pEMC vector with a neomycin-resistant (NeoR) cassette flanked by FRT sites and additional KpnI and EcoRV digestion sites for Southern blotting [Fig. S1C]. The correctly targeted clones have the NeoR upstream of the R3016H mutation site (CGT(Arg)-> CAT(His)) in exon 62 [Fig. S1C and S1E] and were identified by Southern Blotting (EcoRV+KpnI digestion, a 3' probe (generated 5'-TCT CCT GGC TAC ATG CTA-3' and 5'-AAC ACT CAG CCG TCG TC-3') [Fig. S1C and S1D]. The germline and targeted bands are ~13.1 kb and 4.1 kb, respectively [Fig S1D]. The mutation was confirmed by Sanger sequencing [Fig. S1E]. The resulting chimeras were bred with $Rosa26a^{FLP/FLP}$ mice (the Jackson Laboratory; stock no. 003946) to remove the NeoR cassette. Two independently targeted clones were injected for germline transmission and discussed together thereafter. Genotyping primers are 5'- CGC ACA GTG TCG TCT G-3' and 5'-CGT GCC TTT TAA TTA TGT AG-3' and Atm^{R} allele = 592 bp vs Germline= 474 bp. Only 129/sv $Atm^{R/R}$ mice were used in this study. All animal procedures were approved by the Institutional Animal Care and Use Committee at Columbia University Irving Medical Center.

In Vitro Kinase Assay

The wild-type Flag-tagged ATM was a gift from Dr. Michael Kastan and the R3008H and D2889A versions were made using Quikchange mutagenesis (Stratagene). Recombinant human ATM was made by transient transfection of expression constructs into 293T cells using calcium phosphate and purified as described previously (29). ATM kinase assays with MRN and DNA were performed with 1.35 nM ATM, 6.25 nM GST-p53 substrate, 75 nM

MR, 100 nM Nbs1, and 140 nM linear double-stranded DNA as indicated in the figure legends. Kinase assays were performed in kinase buffer (50 mM HEPES, pH 7.5, 50 mM potassium chloride, 5 mM magnesium chloride, 10% glycerol, 1 mM ATP, and 1 mM DTT) for 90 min at 30 °C in a volume of 40 μl as described previously (2). Kinase assays with oxidation were performed with 817 μM hydrogen peroxide (H2O2) (Thermo Fisher Scientific, H325-100), 2.7 nM ATM, and approximately 50 μM dithiothreitol (DTT). Phosphorylated p53 (pS15) was detected as described previously (30) using a phospho-specific antibody (Calbiochem, PC461).

Immunofluorescence

Mice were transcardially perfused with 4% paraformaldehyde (PFA), and tissue was cryoprotected in 25% PBS-buffered sucrose solution, embedded in O.C.T. and sectioned sagittally at 10μm using an HM500M cryostat (Microm). Immunohistochemistry was performed after antigen retrieval (HistoVT One, Nacalai USA). The following primary antibodies were used: phospho-H2ax-Ser-139 (1:500, Cell Signaling, #2577); NeuN (1:500, Chemicon, MAB377), and PCNA (1:500, Santa Cruz, SC-56), and Cy3 conjugated secondary antibodies (Jackson Immunologicals) were used for fluorescent visualization and counterstained with 4',6-diamidino-2-phenylindole (DAPI) (Vector Laboratories). Three independent tissue samples from each genotype were stained and analyzed and one representative picture is shown for each genotype.

Lymphocyte development and Class switch recombination

Lymphocyte development and *in vitro* CSR were performed as described before (10,31,32). Hematopoietic cells from 5–8 week mice were stained and analyzed on a FACS Calibur flow cytometer (BD Biosciences). The antibodies are: PE-CD4 (clone GK1.5, BD Pharmingen, 553730), FITC-CD8α (clone 53–6.7, BioLegend, 100705), APC-TCRβ (clone H57-597, BD Pharmingen, 553174), PE/Cy7 TER-119 (clone TER-119, BioLegend, 116222), FITC-CD43 (clone S7, BD Pharmingen, 553270), PE-Cy5-B220 (clone RA3-6B2, BD Pharmingen, 553091) and PE-IgM (Southern Biotech, 1020-09). For *in vitro* CSR, $CD43^{-}$ splenic cells (anti-CD43 magnetic beads, Miltenyi, 130-049-801) were cultured (~1×10^6 cells ml^{-1}) in RPMI (Gibco, 11875-093), serum supplements (10,31,32), IL-4 (20 ng/mL; R&D, 404-ML-050), and anti-CD40 (1 μg/mL; BD Bioscience, 553721) and analyses with FITC-conjugated IgG1 (clone A85-1, BD Pharmingen, 553443) and PECy5-conjugated B220 (clone RA3-6B2, BD Pharmingen, 553091). FlowJo software package was used for data analyses

Murine embryonic fibroblasts culture, proliferation analyses, and small chemicals

Murine embryonic fibroblasts (MEFs) were harvested at embryonic day 14.5 and cultured in DMEM (Gibco, 12430-054) with 15% fetal bovine serum. Tert-Butyl Hydroperoxide (TBH), cells treated cells were incubated in 2-mercaptoethanol free medium. SV40 antigens immortalized the MEFs (33). MEF proliferation was measured by CellTiter Glo (Promega, G7572, 2×10^3 cells/well on 96 wells) on a GloMax microplate reader (Promega). The relative growth was plotted as the fold increase over the first day [noted as day 0]. B cell proliferation was analyzed using the Cell Trace Violet (CTV) (ThermoFisher Scientific, C34557) and collected on an LSRII flow cytometer (BD Biosciences). Following chemicals

were used: Camptothecin (CPT) (Calbiochem, 208925), Etoposide (EtOP) (Sigma, E1383), TBH solution (Luperox TBH70X, Sigma, 458139), Colcemid (KryoMAX™ Colcemid™, Gibco, 15212-012), and Neocarcinostatin (NCS) (Sigma, N9162).

Cell cycle analyses

For G1/S checkpoint, MEFs were irradiated at 0 or 5 Gy and recovered for 12 hours before pulse-labeled with 10 μM 5-Bromo-2′-deoxyuridine (BrdU, Sigma, B9285) for 30 minutes, stained with anti-BrdU kit (BD Pharmingen, 556028) and propidium iodide (PI) (Sigma, P4170) + Rnase A (Sigma, 10109169001). For G2/M checkpoint, MEFs were irradiated with 0 or 10 Gy, incubated with 100 ng/ml of Colcemid for 3 hours, fixed with 70% ethanol, and stained with anti-phospho Histone H3 (S10) (pH3) antibody (EDM Millipore, 06–570). To combine the anti-pH3 and BrdU staining [Fig. 5D and 5E], the 2.5 days activated B cells were pulse treated with NCS (100 ng/mL) for 1 hour and collected after 3 hours with Colcemid (100 ng/ml final) and 30 min with BrdU(10 μM). Cells were analyzed on an Attune NxT flow cytometer (Thermo Fisher Scientific).

Western blotting and antibodies

Whole-cell extracts (WCEs) were prepared using modified RIPA buffer (150 mM sodium chloride, 10 mM Tris–hydrogen chloride pH 7.4, 0.1% sodium dodecyl sulfate, 0.1% Triton X-100, 1% sodium deoxycholate, 5 mM ethylenediaminetetraacetic acid) with protease inhibitor cocktail (Roche, 11697498001). SDS-PAGE and immunoblots were performed following standard protocols. Primary antibodies are: anti-ATM (Sigma, A1106), anti-pATM S1981 (Cell Signaling, 4526), anti-pKAP1 S824 (Abcam, ab70369), anti-KAP1 (Cell Signaling, 4124), anti-CHK2 (BD Biosciences, 611570), anti-pH2AX Ser139 (Cell Signaling, 9718S), anti-H2AX (Millipore, 07–627), anti-Vinculin (Millipore, 05–386), anti-β-actin (Sigma, A1978) and anti-αTubulin (Calbiochem, CP06).

Metaphase spreads and telomere-FISH (T-FISH)

Metaphases were collected from activated B cells at 4.5 days after stimulation after 2 hours with Colcemid (KaryoMax™ Colcemid™ Solution, GIBCO, 100 ng/ml final) and stated with Telomere-PNA probe (34). The slides were counterstained with Vectashield mounting media containing DAPI (Vector Laboratories, H-1200-10) and analyzed on a Carl Zeiss AxioImager Z2 microscope equipped with a CoolCube 1 camera and a 63/1.30 oil objective lens, driven by Metafer4 and the ISIS fluorescence image software (MetaSystems).

Live cell imaging and fluorescence recovery after photobleaching (FRAP)

U2OS cells with stable shRNA ATM knockdown (U2OS shATM) and plasmids encoding shRNA-resistant human ATM-WT and ATM-KD (pcDNA3; NotI-XhoI containing the entire ORF) were provided by Dr. Christopher Bakkenist (20). We inserted a GFP tag and the SV-40 nuclear localization sequence (NLS) at the N-terminus of ATM (GFP-ATM and GFP-ATM KD). The R3008H mutation was introduced using: FWD 5’- CAA CAA AGT AGC TGA ACA TGT CTT AAT GAG ACT AC-3’ and REV 5’- GTA GTC TCA TTA AGA CAT GTT CAG CTA CTT TGT TG-3’ (GFP-ATM R3008H and GFP-ATM KD/R3008H). For live-cell imaging, U2OS shATM were transiently transfected GFP-ATM plastic with

Lipofectamine 2000 (Invitrogen, 11668019). Two days (48 hours) later, the cells were incubated with BrdU (10 μM) for 16–18 hours before imaging. Laser micro-irradiation and time-lapse imaging were conducted via the NIS Element High Content Analysis software (Nikon Inc) using a 405nm laser (energy level ≅500 μW for a ~0.8μm diameter region) (32,35,36). Relative fluorescence intensity = ratio of the mean intensity at the micro-irradiation sites / the mean nuclear intensity. Fiji: Image J software was used for data analyses. For FRAP, photobleaching with a GFP-specific 488 nm laser (for a ~1.2μm diameter region) was performed at 5 minutes after initial micro-irradiation when the relative intensity of the ATM foci was at its peak, and the fluorescence recovery was documented every 2 seconds for up to 60 seconds as previously described (35,36). Normalized fluorescence intensity for each time point was determined by setting the intensity immediately before and after photobleaching as 100% and 0%, respectively. The maximal recovery (or mobile fractions) and $t_{1/2}$ were calculated based on earlier publications with minor modifications (36). The dissociation constants (Kd) were calculated using the Prism software (GraphPad Software, La Jolla California USA) assuming the one-binding site model. More than 10 cells were acquired and analyzed for each technical repeat. At least two and often three independent technical repeats were performed.

Results

Generation and characterization of mouse models with R3016H Atm mutation *in vivo*.

Homologous targeting was used to introduce the R3016H (CGT-> CAT) mutation [Fig. S1C] to Atm locus in ES cells. The targeted clones were identified by Southern blotting [Fig. S1D], and confirmed by Sanger sequencing [Fig. S1E] before injection. $Atm^{R/R}$ mice express Atm protein at comparable levels to $Atm^{+/+}$ control but lack ionizing radiation (IR) induced phosphorylation of Kap1, H2ax, or Chk2 [Fig. 1E]. ROS-inducing agent TBH also can not induce Kap1 or Chk2 phosphorylation in $Atm^{R/R}$ cells [Fig. 1F]. A much-attenuated activation of Atm-R3018H protein is evident after prolonged treatment with TBH (2–4hr) [Fig. 1F]. Purified human ATM-R3008H also cannot be efficiently activated by MRN+DNA (DNA damage) [Fig. S1F] or H2O2 (ROS generating agents) [Fig. S1G]. When reducing agent DTT was omitted from the reaction buffer, purified ATM-R3008H protein showed reduced yet significant basal activity toward a p53 peptide [Fig. S1H], suggesting that the R3008H mutation compromised ATM activation without abrogating its intrinsic kinase activity. $Atm^{+/R}$ mice were born at the expected rate, normal size, and fertile[Fig. 1G and 1I], suggesting that it is not a classical dominant-negative allele. In contrast to the embryonic lethality of $Atm^{KD/KD}$ mice, $Atm^{R/R}$ mice were born alive, but under-represented ($p<0.0001$) [Fig. 1G], and smaller [Fig. 1H and 1I] than $Atm^{-/-}$ controls. Adolescent $Atm^{R/R}$ mice (1–6 weeks) gain weight normally after birth [Fig. S1I].

The 2–4 weeks old $Atm^{R/R}$ mice have notably short noses [Fig. 2A]. The eye-to-nose/eye-to-eye distance is significantly smaller in $Atm^{R/R}$ mice than $Atm^{+/+}$ and $Atm^{-/-}$ mice [Fig. 2B]. Yet, the rotarod test on three-week-old and six-week-old $Atm^{R/R}$ mice revealed similar defects in $Atm^{R/R}$ and $Atm^{-/-}$ mice with no craniofacial defect [Fig. 2C]. Histological analyses of two-week-[Fig.2D] and eight-week-old [Fig. 2E] $Atm^{R/R}$ mice also show no major changes in γH2ax staining or PCNA (S phase marker). Lig4-deficient neurons

accumulate more γH2ax, while Atm-deleted neurons also show no measurable accumulation of γH2ax(37,38) [Fig.2D]. Thus, $Atm^{R/R}$ mice were born alive with idiopathic craniofacial defects that do not correlate with additional behavior or histological changes beyond those on the $Atm^{-/-}$ mice.

$Atm^{R/R}$ mice display defects in early lymphocyte development and IgH CSR.

Next, we analyzed lymphocyte development. B cell development in both $Atm^{R/R}$ and $Atm^{-/-}$ mice are largely normal [Fig. S2A and S2B]. T cells from $Atm^{R/R}$ and $Atm^{-/-}$ mice show a prominent blockade at the CD4+CD8+ double-positive (DP) to CD4+ or CD8+ single-positive (SP) transition [Fig. 3A, 3B, and S2C] and decreased surface TCRβ levels [Fig. 3A], consistent with defects in Vα-Jα recombination described for Atm-deficiency (8). Consequently, total thymic cellularity is also decreased in $Atm^{R/R}$ mice [Fig. S2C]. The extent of all T cell development defects in $Atm^{R/R}$ mice are largely comparable to those of $Atm^{-/-}$ mice, despite a statistically significant but at most moderate improvement of SP/DP ratio [Fig. 3A, 3B, and S2C]. To examine CSR, purified splenic B cells were activated in the presence of anti-CD40 and IL-4, which stimulate CSR to IgG1 and IgE. Both $Atm^{R/R}$ and $Atm^{-/-}$ B cells showed a > 50% decrease in IgG1 switching [Fig. 3C and 3D]. At day 4.5, $Atm^{R/R}$ B cells show a statistically significant, but very moderate improvement of IgG1 switching than the $Atm^{-/-}$ B cells [Fig. 3C and 3D]. No statistically significant difference in IgG1 CSR was noted at day 3.5 after stimulation [Fig. 3C and 3D]. To understand this “late” switching in $Atm^{R/R}$ B cells, we performed CTV labeling and plotted the frequency of IgG1 CSR in $Atm^{R/R}$ and $Atm^{-/-}$ B lymphocytes by cell division. However, no significant proliferation defects or preference for IgG1 CSR at later days were noted between in $Atm^{R/R}$ and $Atm^{-/-}$ B lymphocytes [Fig. S2D and S2E].

Since the IgH gene resides near the telomere end of murine chromosome 12, telomere FISH analyses have been used to visualize and quantify CSR associated DNA repair defects in activating B cells (10,32,34). Telomere FISH can recognize two types of breaks – chromosome breaks involving both sister chromatids and chromatid breaks involving one of the two sister chromatids (10,32,34) [Fig. 3G]. Chromatid breaks occur during or after DNA replication, reflecting the different fates of the two sister chromatids, while chromosome breaks are initiated in G1 cells (34). In $Atm^{-/-}$ B cells, the CSR associated IgH breaks were almost all chromosome breaks (34). Telomere FISH analyses show that both $Atm^{R/R}$ and $Atm^{-/-}$ B cells have increased metaphases with breaks (either kind) [Fig. 3E, 3G, S3], with a very moderate yet significant lower frequency of chromosome breaks in the $Atm^{R/R}$ cells [Fig. 3F, 3G, and S3]. In addition to breaks, telomere FISH can also reveal telomere instability, characterized by fragmented telomere signals [Fig. 3G]. Telomere fragility has been noted in Pot1a or ATR deficient cells and linked to replication stress at the telomeres (36,39). $Atm^{R/R}$ B cells have at most a moderate increased frequency of telomere fragility [Fig. 3G, 3H, and S3]. Taken together, lymphocyte analyses of $Atm^{R/R}$ mice confirmed that lymphocyte-specific gene rearrangement is significantly compromised in $Atm^{R/R}$ mice. The extent of repair defects is quite comparable to those seen in $Atm^{-/-}$ mice.

Spontaneous lymphomas were significantly delayed in *Atm*$^{R/R}$ mice

Atm$^{-/-}$ mice routinely succumbed to thymic lymphomas by 4 months of age ($t_{1/2}$=115 days) [Fig. 4A and 4C]. Despite the ongoing genomic instabilities noted above, the expression of Atm-R3016H significantly lengthened overall life expectance ($t_{1/2}$=211 days) [Fig. 4A] and the occurrence of thymic lymphomas specifically in both *Atm*$^{-/R}$ mice ($t_{1/2}$=194 days overall, and 190 days for thymic lymphomas only, $p<0.01$, Mantel-Cox test) and *Atm*$^{R/R}$ mice ($t_{1/2}$=211 days overall, and 183 days for thymic lymphomas, $p<0.0001$, Mantel-Cox test) [Fig. 4C]. *Atm*$^{+/+}$ mice in pure 129sv background rarely develop spontaneous tumors before 1 year (365 days) of age, indicating that R3008H mutation confers the partial loss of ATM tumor suppressor function. Moreover, *Atm*$^{R/R}$ and *Atm*$^{-/R}$ mice displayed a shift in overall tumor types [Fig. 4B]. In addition to the (CD3 low) thymic lymphomas [Fig. 4D], the *Atm*$^{-/R}$ and *Atm*$^{R/R}$ mice developed other hematologic malignancies (*e.g.,* pro-B cell lymphomas with the expansion of $B220^{+}IgM^{-}CD43^{+}$cells, Fig. 4E). Thymus development peaks at 1 month and attenuates afterward. The older *Atm*$^{R/R}$ and *Atm*$^{-/R}$ mice that escaped lethal thymic lymphomas, eventually developed other hematological malignancy and sarcomas later in life [Fig. 4A]. Those findings suggest that a mechanism beyond the programmed DSBs repair defects might contribute to the delayed lymphomagenesis and craniofacial abnormalities in *Atm*$^{R/R}$ mice.

Atm$^{R/R}$ cells have defects in IR induced cell cycle checkpoints like *Atm*$^{-/-}$ cells

So next, we analyzed the proliferation and the cell cycle checkpoints in *Atm*$^{R/R}$ and *Atm*$^{-/-}$ MEFs and B cells. Both *Atm*$^{R/R}$ and *Atm*$^{-/-}$ MEFs grew significantly slower without a major difference between the two alleles [Fig. 5A], had a reduced S phase (BrdU+) fraction [Fig. 5B and Fig. S4A], and a decreased mitotic fraction (pH3+) among all G2/M cells [Fig. 5C and 5D], suggesting a delayed mitotic entry. ATM regulates DNA damage-induced G1/S checkpoint upstream of p53 and the G2/M checkpoint upstream of CHK2 (40). Both functions require DNA damage-induced kinase activity of ATM. Accordingly, both *Atm*$^{R/R}$ and *Atm*$^{-/-}$ B cells lost the genotoxic-induced G2/M checkpoint [Fig. 5E].

Atm$^{R/R}$ and *Atm*$^{-/-}$ primary MEFs showed defects in ionizing-radiation induced G1/S [Fig. S4A] and G2/M checkpoints [Fig. 5F and S4B], consistent with the lack of IR-induced acute activation of Atm-R3016H [Fig. 5H and 5I, at 0.5 and 1 hour]. Thus, those analyses in MEFs and B cells suggest that DNA damage-induced acute checkpoint activation is similarly affected in *Atm*$^{R/R}$ and *Atm*$^{-/-}$ mice in general.

Atm$^{R/R}$ cells can respond to chronic DNA damage

While IR-induced ‘transient’ DNA damage and ATM activation, we noted the prolonged TBH treatment (2–4 hours) evoked significant activation of Atm-R3016H [Fig. 1F]. To determine whether Atm-R3016H can respond to ROS induced checkpoint activation, we treated *Atm*$^{R/R}$ and *Atm*$^{-/-}$ primary MEF cells with TBH, a ROS inducer. As shown in Figure 1F, acute treatment with TBH, even at a high dose (700 μM), did not induce significant Chk2 phosphorylation, but the extended treatment of 2 and 4 hours caused noticeable Atm-R3016H activation beyond the loss of Atm. Thus, we treated primary MEFs for 4 hours with 200 μM TBH, which induced a ~40% reduction of the mitotic entry in *Atm*$^{+/+}$ MEFs [Fig. 5F]. While *Atm*$^{R/R}$ and *Atm*$^{-/-}$ MEFs fail to activate the G2/M checkpoint

upon radiation, $Atm^{R/R}$ MEFs, and, to a lesser extent, $Atm^{-/-}$ MEFs show a stronger G2/M arrest in response to TBH than $Atm^{+/+}$ MEFs [Fig. 5F and S4B].

To determine whether this difference reflects the ability of Atm-R3016H to respond to chronic stress in general or ROS specifically, we treated $Atm^{R/R}$ cells with DNA damage agents for 4 hours. Although very much diminished, $Atm^{R/R}$ cells could phosphorylate Chk2 beyond the levels observed in $Atm^{-/-}$ cells [Fig. 5G]. Those findings are consistent with the retention of basal kinase activity, but the lack of efficient DNA damage- and ROS-induced activation of ATM-R3008 *in vitro* [Fig. S1F, S1G, and S1H]. We proposed that chronic activation of Atm-R3016H might contribute to the delayed lymphomagenesis and craniofacial defects in $Atm^{R/R}$ mice.

R3008H mutation rescues exchange defects of ATM KD protein

To determine whether the R3008H mutation affects ATM-MRN interaction to attenuate ATM activation, we expressed shRNA resistant GFP-tagged ATM-R3008H or ATM-WT in U2OS shATM cells [Fig. S4C]. Both ATM-R3008H and the previously characterized ATM-KD could be efficiently recruited to the site of DNA damage [Fig. 6A, 6B and 6C]. Live-cell imaging further showed that the recruitment kinetics [Fig. 6B] and relative fluorescence intensity [Fig. 6C] of damage-induced foci formed by ATM-R3008H and ATM-KD were indistinguishable from ATM-WT. Correspondingly, purified ATM-R3008H can efficiently bind to both MRN and MR [Fig. S4D and S4E]. In an earlier study, we found that the ATR kinase inhibitors affect ATR exchange without affecting the initial recruitment of ATR at the DNA damage site (36,41). To test whether this is also true for ATM, we measured fluorescence recovery after photobleaching (FRAP) at 5 minutes after initial micro-irradiation, when the ATM foci intensity reaches a plateau [Fig. 6B]. ATM-KD showed a moderate, yet consistent, delay of exchange evidenced by a significantly delayed $t_{1/2}$ (9.46 ± 1.91 vs. 7.56 ± 1.79 for ATM-WT, p=0.02, unpaired two-tailed t-test) and moderate reduction of maximal recovery (0.67 ± 0.08 vs. 0.75 ± 0.1 for ATM-WT, p=0.05, unpaired two-tailed Student's t-test) [Fig. 6D – 6F], suggesting that ATM kinase activity might also be linked to ATM exchange. Surprisingly, ATM-R3008H displays no exchange defects ($t_{1/2}$=7.98 ± 1.83 vs. 7.56 ± 1.79 for ATM-WT, p=0.59, unpaired two-tailed Student's t-test) and even higher maximal recovery (0.91 ± 0.05 vs. 0.75 ± 0.1 for ATM-WT, p<0.001 unpaired two-tailed Student's t-test) [Fig. 6D – 6F]. Based on these findings, we propose a model in which the PRD is critical in connecting ATM activation with the dynamic exchange of ATM at the DNA damage sites. The R3008H mutation at the Kα10 helix [Fig. 1B and 1C] abrogates this link, impairing ATM activation and high-affinity engagement of ATM with the MRN-DNA complex. Consistent with this hypothesis, ATM carrying both R3008H and KD mutations at the same cDNA can exchange effectively, suggesting R3008H mutation rescued the exchange defects in ATM-KD *in cis* [Fig. 6D - 6F]. Together, our data support a model in which the R3008H mutation interferes with ATM activation by impairing the allosteric changes that link ATM kinase activation and ATM exchange.

Discussion

The embryonic lethality of $Atm^{KD/-}$ mice and the enrichment of missense ATM mutation in cancers suggest that the frequency of pathogenic ATM mutations in cancer might be greatly under-estimated. The much more severe genomic instability of $Atm^{KD/-}$ cells suggests that the presence of ATM protein without kinase activity might physically block DNA processing and/or repair (3,10,11). Due to the large size, functional validation of cancer-associated ATM mutations has been technically challenging. Most genetic screens only consider mutations identified in A-T patients as bonafide ATM-inactivation mutations. Missense mutations in the PRD domain are frequently found in human cancer. Here we showed that $Atm^{R/R}$ mice carrying a PRD domain missense mutation are viable and express a stable ATM protein that cannot be activated by either DNA damage or ROS. This is unexpected, given the embryonic lethality of $Atm^{KD/KD}$ mice, and suggest that the kinase-dependent structural function of ATM can be uncoupled from the phosphorylation of its substrates, including itself. Instead, we propose that ATM activation and the completion of the phosphoryl group transfer might be coupled with ATM exchange. Specifically, our and prior FRAP analyses provide direct evidence for the rapid exchange of ATM at the DNA damage sites (42). Mechanistically, structural analyses of Tel1, the yeast homolog of ATM, suggest that the PRD regulates the cap that limits access of the substrate and ATP to the well-positioned catalytic center (24–26). Based on the successful development of $Atm^{R/R}$ mice vs. the embryonic lethality of $Atm^{KD/KD}$ mice, and the ability of R3008H mutation to rescue the exchange defects of ATM-KD, we propose a model in which the PRD supports ATM activation by allowing the substrate to engage with the catalytic center, where this engagement is necessary to lock Atm-KD, where it prevents replication-associated DNA repair. At the molecular level, the arginine 3008 residue is one of the several conserved basic amino acids spaced 3–4 aa apart within the Kα10 helix implicated in stabilizing the helix structure by providing stacking interaction (43) [Fig. 1B and 1C]. Thus, R3008H mutation might cause partial denaturation of the Kα10 helix and impairs the “cap (PRD-I)” opening necessary for ATM activation, thereby diminishing the substrates’ and ATP’s access to the catalytic loop. In this role, the R3008H mutation reduces the unproductive engagement of the ATM-KD protein with its substrate and preventing stalling. This mechanism would also explain why the R3008H mutation (or R3016H of mouse Atm) abolished acute activation of ATM necessary for DNA repair but retained some basal activity to phosphorylate CHK2 during chronic stress, which might contribute to the delayed tumor onset. Alternatively, R3008H might alter substrates specificity, as IR induced Atm-S1987 auto-phosphorylation seems to be less affected than Kap1 phosphorylation, and in chronically stressed $Atm^{R/R}$ cells, Chk2 phosphorylation is less affected than Kap1 phosphorylation. In this case, we caution that in addition to ATM activity, the phosphorylation levels of ATM substrates at any given time are also influenced by the availability of other kinases (*e.g.*, DNA-PKcs), the half-life of the phosphorylated proteins, and the accessibility to phosphatase.

In A-T patients, Ataxia is largely uniform, but immunodeficiency and cancer risk vary extensively. Using inbred mouse models, our data, and previous analyses of Atm-KD mice (summarized in Table S1) support a specific contribution of ATM mutation in the diverse immunological and cancer predisposition phenotypes beyond the genetic background of the

patients. Specifically, ATM kinase activity affects clean DSB repair, which is similarly affected by null, KD, and R3008H mutations and correlates with lymphocyte-specific recombination defects. We note that lymphocyte development can also be affected by proliferation (as those caused by Atm-KD) in addition to rearrangement defects. In the absence of ATM kinase activation, the expression level of the inactive ATM protein and the type of mutation (kinase-dead or inactivation mutation - R3008H) work together to the stalling of ATM at DNA damage sites and the genotoxicity associated with the expression of kinase-dead ATM. In this regard, we speculate that the craniofacial defects of $Atm^{R/R}$ mice without an additional decline of motor neural function might reflect proliferation defects in olfactory neurons that undergo extensive post-natal neurogenesis.

Finally, the difference between kinase-dead vs. null is not limited to ATM kinase but also observed for DNA-PK (44,45) and ATR (36,41). In each case, the cytotoxicity is specific to the DNA substrates that recruit and activate the respective kinases – DSBs for DNA-PKcs and single-stranded DNA for ATR. In the case of DNA-PKcs, the deletion of KU, which recruits DNA-PKcs to the DNA ends, rescues the embryonic lethality of $DNA\text{-}PKcs^{KD/KD}$ mice (44–46). The dynamic exchange of ATR at RPA coated single-strand DNA is markedly reduced by ATR specific inhibitors (36,41), suggesting that the coupling between catalysis and the release of the kinase might be a common feature for all PIKK. The sequence corresponding to the Kα10 also exists in ATR, DNA-PKcs, and the related mTOR (47). Therefore, the phenotype and the mechanism of exchange regulated by R3008H identified here can potentially be applied to understand the kinase-dependent regulation of other PIKKs.

Supplementary Material

Refer to Web version on PubMed Central for supplementary material.

Acknowledgments

We thank members of the Zha lab for discussion, Dr. Bakkenist for providing ATM plasmids and ATM knock-down U2OS cells, Dr. Claudio Scuoppo for comments on the manuscript. This work was supported by the NIH/NCI grants R01CA158073, R01CA215067, R01CA226852, and P01 CA174653 to SZ. SZ is a Leukemia Lymphoma Society Scholar. LMH was supported by NIH/NCI T32 CA09503-29. J-H L and TP were supported by the Howard Hughes Medical Institute. PJM is supported by the NIH (NS-37956, CA-21765), the CCSG (P30 CA21765), and the American Lebanese and Syrian Associated Charities of St. Jude Children's Research Hospital. DW and JX were supported by NIH GM102362. This research was funded in part through the NIH/NCI Cancer Center Support Grant P30CA013696 to the Herbert Irving Comprehensive Cancer Center of Columbia University.

References

1. Shiloh Y ATM: expanding roles as a chief guardian of genome stability. Experimental cell research 2014;329:154–61 [PubMed: 25218947]
2. Gilad S, Khosravi R, Shkedy D, Uziel T, Ziv Y, Savitsky K, et al. Predominance of null mutations in ataxia-telangiectasia. Hum Mol Genet 1996;5:433–9 [PubMed: 8845835]
3. Yamamoto K, Wang J, Sprinzen L, Xu J, Haddock CJ, Li C, et al. Kinase-dead ATM protein is highly oncogenic and can be preferentially targeted by Topoisomerase I inhibitors. Elife 2016;5
4. Barlow C, Hirotsune S, Paylor R, Liyanage M, Eckhaus M, Collins F, et al. Atm-deficient mice: a paradigm of ataxia telangiectasia. Cell 1996;86:159–71 [PubMed: 8689683]

5. Xu Y, Ashley T, Brainerd EE, Bronson RT, Meyn MS, Baltimore D. Targeted disruption of ATM leads to growth retardation, chromosomal fragmentation during meiosis, immune defects, and thymic lymphoma. Genes Dev 1996;10:2411–22 [PubMed: 8843194]
6. Elson A, Wang Y, Daugherty CJ, Morton CC, Zhou F, Campos-Torres J, et al. Pleiotropic defects in ataxia-telangiectasia protein-deficient mice. ProcNatlAcadSciUSA 1996;93:13084–9
7. Borghesani PR, Alt FW, Bottaro A, Davidson L, Aksoy S, Rathbun GA, et al. Abnormal development of Purkinje cells and lymphocytes in Atm mutant mice. ProcNatlAcadSciUSA 2000;97:3336–41
8. Zha S, Bassing CH, Sanda T, Brush JW, Patel H, Goff PH, et al. ATM-deficient thymic lymphoma is associated with aberrant tcrd rearrangement and gene amplification. Journal of Experimental Medicine 2010;207:1369–80
9. Herzog KH, Chong MJ, Kapsetaki M, Morgan JI, McKinnon PJ. Requirement for Atm in ionizing radiation-induced cell death in the developing central nervous system. Science 1998;280:1089–91 [PubMed: 9582124]
10. Yamamoto K, Wang Y, Jiang W, Liu X, Dubois RL, Lin CS, et al. Kinase-dead ATM protein causes genomic instability and early embryonic lethality in mice. J Cell Biol 2012;198:305–13 [PubMed: 22869596]
11. Daniel JA, Pellegrini M, Lee BS, Guo Z, Filsuf D, Belkina NV, et al. Loss of ATM kinase activity leads to embryonic lethality in mice. J Cell Biol 2012;198:295–304 [PubMed: 22869595]
12. Huang KL, Mashl RJ, Wu Y, Ritter DI, Wang J, Oh C, et al. Pathogenic Germline Variants in 10,389 Adult Cancers. Cell 2018;173:355–70 e14 [PubMed: 29625052]
13. Tal E, Alfo M, Zha S, Barzilai A, De Zeeuw CI, Ziv Y, et al. Inactive Atm abrogates DSB repair in mouse cerebellum more than does Atm loss, without causing a neurological phenotype. DNA Repair (Amst) 2018;72:10–7 [PubMed: 30348496]
14. Bredemeyer AL, Sharma GG, Huang CY, Helmink BA, Walker LM, Khor KC, et al. ATM stabilizes DNA double-strand-break complexes during V(D)J recombination. Nature 2006;442:466–70 [PubMed: 16799570]
15. Zha S, Guo C, Boboila C, Oksenych V, Cheng HL, Zhang Y, et al. ATM damage response and XLF repair factor are functionally redundant in joining DNA breaks. Nature 2011;469:250–4 [PubMed: 21160472]
16. Lumsden JM, McCarty T, Petiniot LK, Shen R, Barlow C, Wynn TA, et al. Immunoglobulin class switch recombination is impaired in Atm-deficient mice. JExpMed 2004;200:1111–21
17. Reina-San-Martin B, Chen HT, Nussenzweig A, Nussenzweig MC. ATM is required for efficient recombination between immunoglobulin switch regions. JExpMed 2004;200:1103–10
18. Panchakshari RA, Zhang X, Kumar V, Du Z, Wei PC, Kao J, et al. DNA double-strand break response factors influence end-joining features of IgH class switch and general translocation junctions. Proc Natl Acad Sci U S A 2018;115:762–7 [PubMed: 29311308]
19. Kozlov SV, Graham ME, Jakob B, Tobias F, Kijas AW, Tanuji M, et al. Autophosphorylation and ATM activation: additional sites add to the complexity. J Biol Chem 2011;286:9107–19 [PubMed: 21149446]
20. Bakkenist CJ, Kastan MB. DNA damage activates ATM through intermolecular autophosphorylation and dimer dissociation. Nature 2003;421:499–506 [PubMed: 12556884]
21. Daniel JA, Pellegrini M, Lee JH, Paull TT, Feigenbaum L, Nussenzweig A. Multiple autophosphorylation sites are dispensable for murine ATM activation in vivo. JCell Biol 2008;183:777–83 [PubMed: 19047460]
22. Pellegrini M, Celeste A, Difilippantonio S, Guo R, Wang W, Feigenbaum L, et al. Autophosphorylation at serine 1987 is dispensable for murine Atm activation in vivo. Nature 2006
23. Guo Z, Kozlov S, Lavin MF, Person MD, Paull TT. ATM activation by oxidative stress. Science 2010;330:517–21 [PubMed: 20966255]
24. Xin J, Xu Z, Wang X, Tian Y, Zhang Z, Cai G. Structural basis of allosteric regulation of Tel1/ATM kinase. Cell Research 2019
25. Wang X, Chu H, Lv M, Zhang Z, Qiu S, Liu H, et al. Structure of the intact ATM/Tel1 kinase. Nature communications 2016;7:11655

26. Yates LA, Williams RM, Hailemariam S, Ayala R, Burgers P, Zhang X. Cryo-EM Structure of Nucleotide-Bound Tel1(ATM) Unravels the Molecular Basis of Inhibition and Structural Rationale for Disease-Associated Mutations. Structure 2020;28:96–104 e3 [PubMed: 31740029]
27. Baretic D, Pollard HK, Fisher DI, Johnson CM, Santhanam B, Truman CM, et al. Structures of closed and open conformations of dimeric human ATM. Science advances 2017;3:e1700933 [PubMed: 28508083]
28. Zha S, Sekiguchi J, Brush JW, Bassing CH, Alt FW. Complementary functions of ATM and H2AX in development and suppression of genomic instability. ProcNatlAcadSciUSA 2008;105:9302–6
29. Lee Y, McKinnon PJ. Responding to DNA double strand breaks in the nervous system. Neuroscience 2006
30. Lee JH, Paull TT. ATM activation by DNA double-strand breaks through the Mre11-Rad50-Nbs1 complex. Science 2005;308:551–4 [PubMed: 15790808]
31. Liu X, Wang XS, Lee BJ, Wu-Baer FK, Lin X, Shao Z, et al. CtIP is essential for early B cell proliferation and development in mice. J Exp Med 2019;216:1648–63 [PubMed: 31097467]
32. Liu X, Shao Z, Jiang W, Lee BJ, Zha S. PAXX promotes KU accumulation at DNA breaks and is essential for end-joining in XLF-deficient mice. Nature communications 2017;8:13816
33. Lee JT, Jaenisch R. Long-range cis effects of ectopic X-inactivation centres on a mouse autosome. Nature 1997;386:275–9 [PubMed: 9069285]
34. Franco S, Gostissa M, Zha S, Lombard DB, Murphy MM, Zarrin AA, et al. H2AX prevents DNA breaks from progressing to chromosome breaks and translocations. MolCell 2006;21:201–14
35. Shao Z, Lee BJ, Rouleau-Turcotte E, Langelier MF, Lin X, Estes VM, et al. Clinical PARP inhibitors do not abrogate PARP1 exchange at DNA damage sites in vivo. Nucleic Acids Res 2020;48:9694–709 [PubMed: 32890402]
36. Menolfi D, Jiang W, Lee BJ, Moiseeva T, Shao Z, Estes V, et al. Kinase-dead ATR differs from ATR loss by limiting the dynamic exchange of ATR and RPA. Nature communications 2018;9:5351
37. Lee Y, Barnes DE, Lindahl T, McKinnon PJ. Defective neurogenesis resulting from DNA ligase IV deficiency requires Atm. Genes Dev 2000;14:2576–80 [PubMed: 11040211]
38. Lee Y, Chong MJ, McKinnon PJ. Ataxia telangiectasia mutated-dependent apoptosis after genotoxic stress in the developing nervous system is determined by cellular differentiation status. JNeurosci 2001;21:6687–93 [PubMed: 11517258]
39. Sfeir A, Kosiyatrakul ST, Hockemeyer D, MacRae SL, Karlseder J, Schildkraut CL, et al. Mammalian telomeres resemble fragile sites and require TRF1 for efficient replication. Cell 2009;138:90–103 [PubMed: 19596237]
40. Shiloh Y, Kastan MB. ATM: genome stability, neuronal development, and cancer cross paths. AdvCancer Res 2001;83:209–54
41. Menolfi D, Zha S. ATM, ATR and DNA-PKcs kinases-the lessons from the mouse models: inhibition not equal deletion. Cell Biosci 2020;10:8 [PubMed: 32015826]
42. Davis AJ, So S, Chen DJ. Dynamics of the PI3K-like protein kinase members ATM and DNA-PKcs at DNA double strand breaks. Cell Cycle 2010;9:2529–36 [PubMed: 20543558]
43. Wang W, Daley JM, Kwon Y, Krasner DS, Sung P. Plasticity of the Mre11-Rad50-Xrs2-Sae2 nuclease ensemble in the processing of DNA-bound obstacles. Genes Dev 2017;31:2331–6 [PubMed: 29321177]
44. Shao Z, Flynn RA, Crowe JL, Zhu Y, Liang J, Jiang W, et al. DNA-PKcs has KU-dependent function in rRNA processing and haematopoiesis. Nature 2020;579:291–6 [PubMed: 32103174]
45. Jiang W, Crowe JL, Liu X, Nakajima S, Wang Y, Li C, et al. Differential phosphorylation of DNA-PKcs regulates the interplay between end-processing and end-ligation during nonhomologous end-joining. Mol Cell 2015;58:172–85 [PubMed: 25818648]
46. Wang XS, Zhao J, Wu-Baer F, Shao Z, Lee BJ, Cupo OM, et al. CtIP-mediated DNA resection is dispensable for IgH class switch recombination by alternative end-joining. Proc Natl Acad Sci U S A 2020;117:25700–11 [PubMed: 32989150]
47. Yang H, Rudge DG, Koos JD, Vaidialingam B, Yang HJ, Pavletich NP. mTOR kinase structure, mechanism and regulation. Nature 2013;497:217–23 [PubMed: 23636326]

Significant Statement

The study functionally characterizes the most common ATM missense mutation R3008H in cancer and identifies a unique role of PI3Kinase regulatory domain in ATM activation.

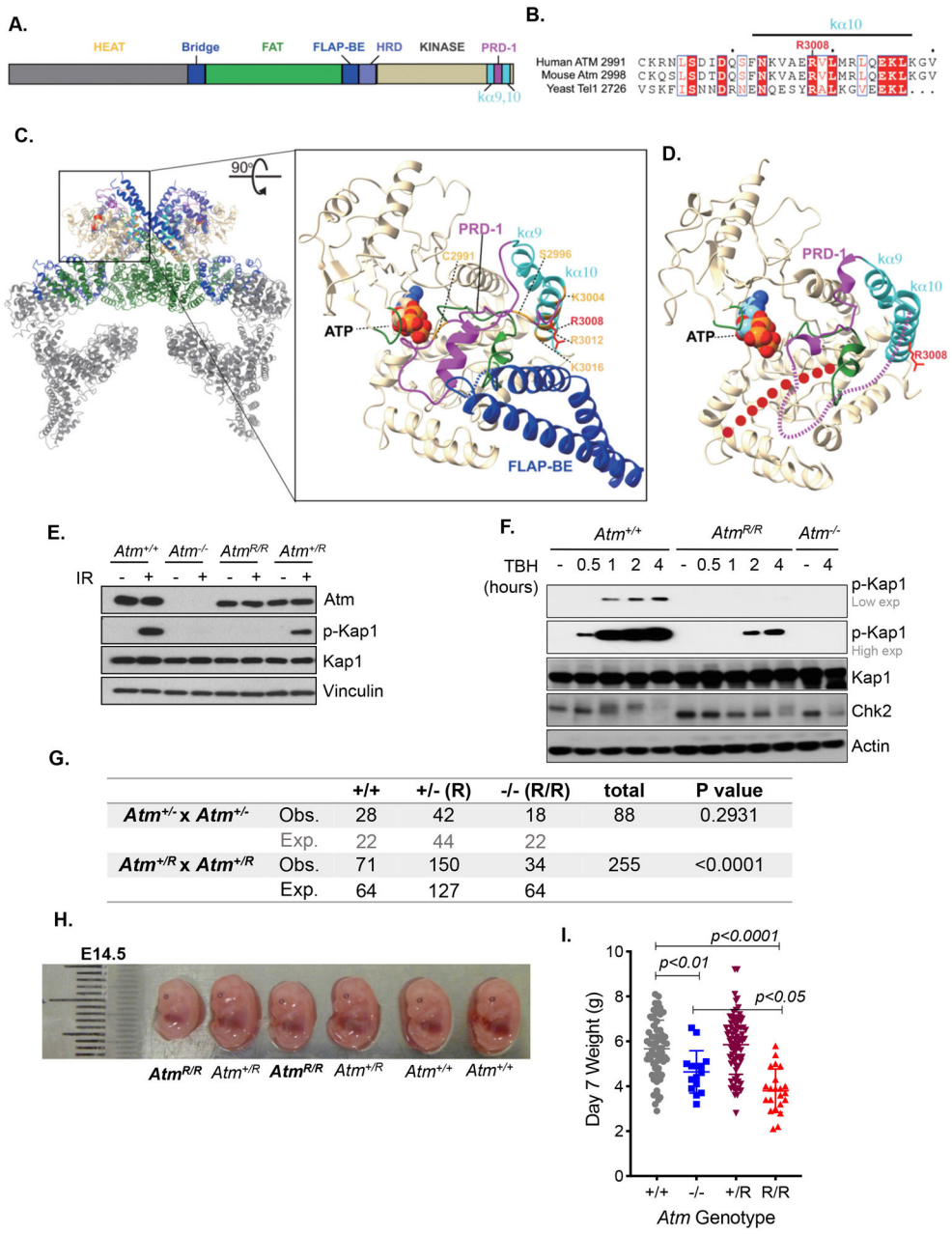

		+/+	+/- (R)	-/- (R/R)	total	P value
***Atm*$^{+/-}$ x *Atm*$^{+/-}$**	Obs.	28	42	18	88	0.2931
	Exp.	22	44	22		
***Atm*$^{+/R}$ x *Atm*$^{+/R}$**	Obs.	71	150	34	255	<0.0001
	Exp.	64	127	64		

Fig 1. The expression of catalytically inactive Atm-R3016H is compatible with embryonic development.

A) Schematic representation of human ATM kinase and its C-terminal portion showing the kinase domain, protein regulatory domain (PRD-1). **B)** Sequence alignment of the kα10 helix, as well as the position of residues C2991, S2996, R3008, and K3016. The positively charged residues on the kα10 helix are marked in orange and the targeted R3008 is in red. **C)** Left, the overall structure of inactive state Tel1, the yeast ortholog of human ATM (PDB ID: 6S8F)(26). Middle, close-up view of kinase domain active sites. The Glycine-rich loop and activation loop are shown in green. The positively charged residues on the kα10 helix are marked in gold and the targeted R3008 is in red. Residues are numbered based on the

sequence of the human ATM protein sequence. **D)** Active state in-silico structure model of ATM (PBDID: 5NP1)(27). The location of ATP was modeled based on the crystal structure of the mTOR FATKIN (PDB ID: 4JSV)(47). The location of the substrate peptide (red spheres) was modeled by superimposing a peptide-bound Cdk2 (PDB ID: 3QHW) onto the ATM active site. The color code is corresponding to Fig.1A. **E)** Western blot analysis of littermate matched primary MEFs collected 2 hours after 5 Gy irradiation. **F)** Western blot analysis of MEFs treated with the ROS-inducing agent TBH (700μM). Cells were collected at the indicated times after TBH treatment. **G)** Expected and observed offspring genotype numbers from intercrosses between $Atm^{+/-}$ (top two rows) or $Atm^{+/R}$ (bottom two rows) mice. The p-value was calculated using the χ^2 test. **H)** Representative images of E14.5 day-old $Atm^{+/+}$, $Atm^{+/R,}$ and $Atm^{R/R}$ embryos. **I)** The weight (gram) of 7 days old $Atm^{+/+}$, $Atm^{-/-}$, $Atm^{+/R}$, and $Atm^{R/R}$ mice (n>=12 for each genotype). On the graph, horizontal lines represent mean ± standard deviation. P-values were calculated using unpaired Student's t-test.

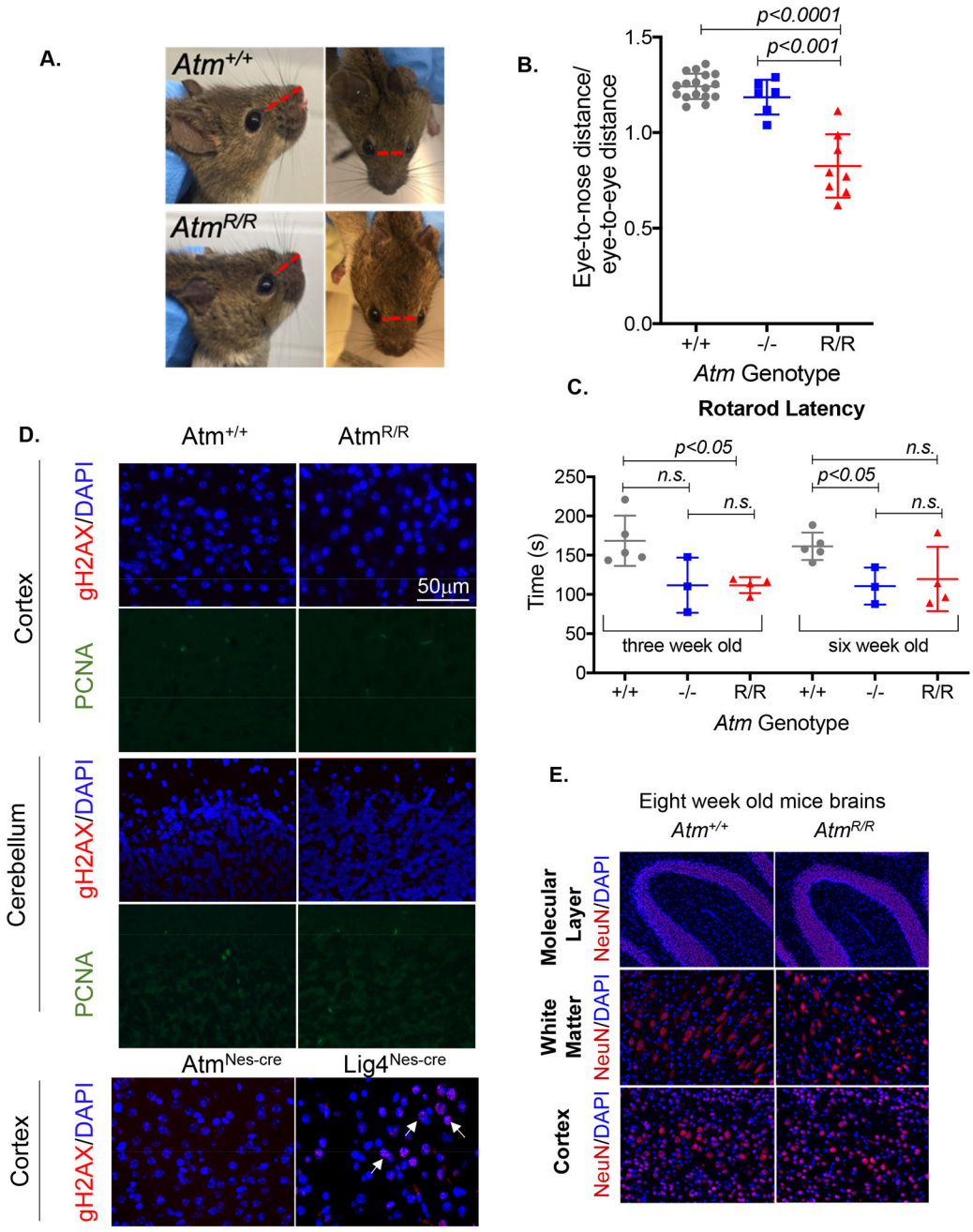

Fig 2. *Atm*$^{R/R}$ mice show craniofacial defects without additional behavioral or histological changes beyond those present in *Atm*$^{-/-}$ mice.

A) Representative images of 2-week old *Atm*$^{+/+}$ and *Atm*$^{R/R}$ mice showing the shortened nose. **B)** Eye-to-nose:eye-to-eye ratios of *Atm*$^{+/+}$, *Atm*$^{-/-}$, and *Atm*$^{R/R}$ mice (n>=6 for each genotype). On the graph, horizontal lines represent mean ± standard deviation. P-values were calculated using unpaired Student's t-test. **C)** Latency(s) before dropping on the rotarod test of three- and six-week-old *Atm*$^{+/+}$ (n=5), *Atm*$^{-/-}$ (n=3), and *Atm*$^{R/R}$ (n=4) mice. On the graph, horizontal lines represent mean ± standard deviation. P-values were calculated using unpaired two-tailed Student's *t*-test. **D)** Cortex and cerebellum sections from two-

week-old $Atm^{+/+}$ and $Atm^{R/R}$ mice were immunostained for γ-H2ax and PCNA. DAPI was used as a nuclear counterstain. Representative stainings of age-matched mice with neuron-specific deletion of Atm ($NestinCre^{+}Atm^{C/C}$) or Lig4 ($NestinCre^{+}Lig4^{C/C}$) were included as controls. **E)** Cortex, white matter, and molecular layer sections from eight-week-old $Atm^{+/+}$ and $Atm^{R/R}$ mice immunostained for NeuN. DAPI was used as a nuclear stain. $p>0.05$ = n.s. (not significant).

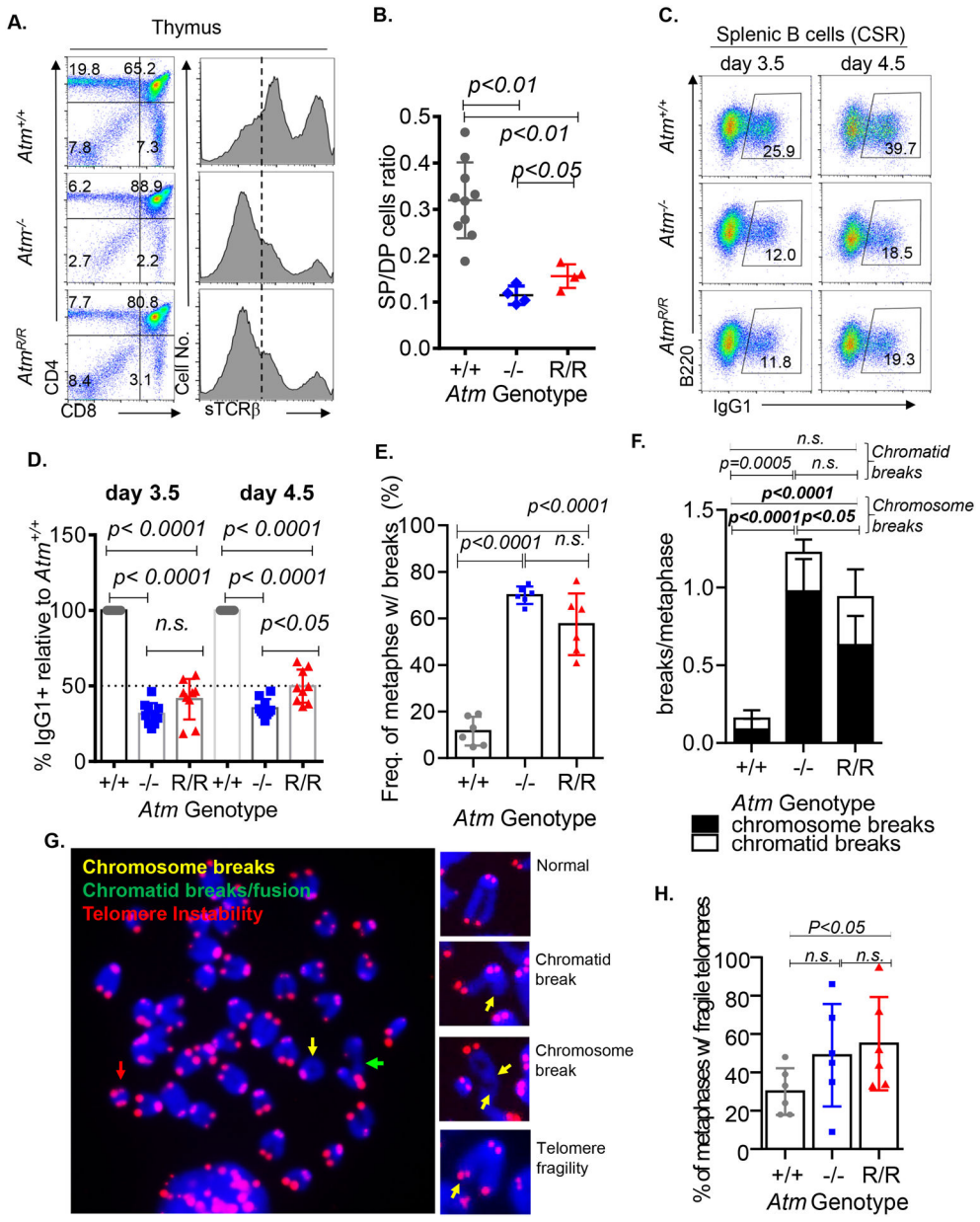

Fig 3. Increased genomic instability and development defects of *Atm*$^{R/R}$ lymphocytes.

A) Representative flow cytometry analyses of thymocytes from *Atm*$^{+/+}$, *Atm* $^{-/-}$, and *Atm*$^{R/R}$ mice. The dotted line shows the median level of surface TCRβ. The percentage of cells in each quadrant are marked on the plots. **B)** Ratios of the total single-positive cells (CD8+CD4− or CD8−CD4+) to double-positive (CD8+CD4+) T cells for *Atm*$^{+/+}$ (n=10) *Atm*$^{-/-}$ (n=5), and *Atm*$^{R/R}$ (n=4) mice. On the graph, horizontal lines represent mean ± standard deviation. **C)** Representative flow cytometry plots for surface IgG1+ frequency in activated B cells from *Atm*$^{+/+}$, *Atm*$^{-/-}$, and *Atm*$^{R/R}$ at the indicated days following CSR stimulation. **D)** The percentage of IgG1+ B cells (relative to WT cells in each experiment; WT set as 100%) in *Atm*$^{+/+}$ (n=5), *Atm*$^{-/-}$ (n=3), and *Atm*$^{R/R}$ (n=5) B cells stimulated to undergo CSR. Bar graphs represent the mean ± standard deviation. Dotted line indicates

50% of WT levels of IgG1 switching. **E)** Frequency of metaphases with cytogenetic abnormalities in splenic B cells of the indicated genotypes. **F)** Frequency of chromatid and chromosome breaks per metaphase in $Atm^{+/+}$, $Atm^{-/-}$, or $Atm^{R/R}$ B cells treated as described. P-values in bold refer to statistics for chromosome breaks and notbolded p-values refer to statistics for chromatid breaks. N=6 for each genotype. **G)** Representative images of different types of cytogenetic abnormalities scored in the context of intact metaphase (left) or as examples (right). **H)** Percentage of metaphases with telomere fragility measured by T-FISH analyses in stimulated B cells from $Atm^{+/+}$, $Atm^{-/-}$, or $Atm^{R/R}$ mice. N=6 for each genotype. **E)**, **F)** and **H)** Bar graphs represent mean ± standard deviation. P-values for **B)**, **D)**, **E)**, **F)**, and **H)** were calculated using unpaired two-tailed Student's *t*-test. p>0.05 = n.s. (not significant).

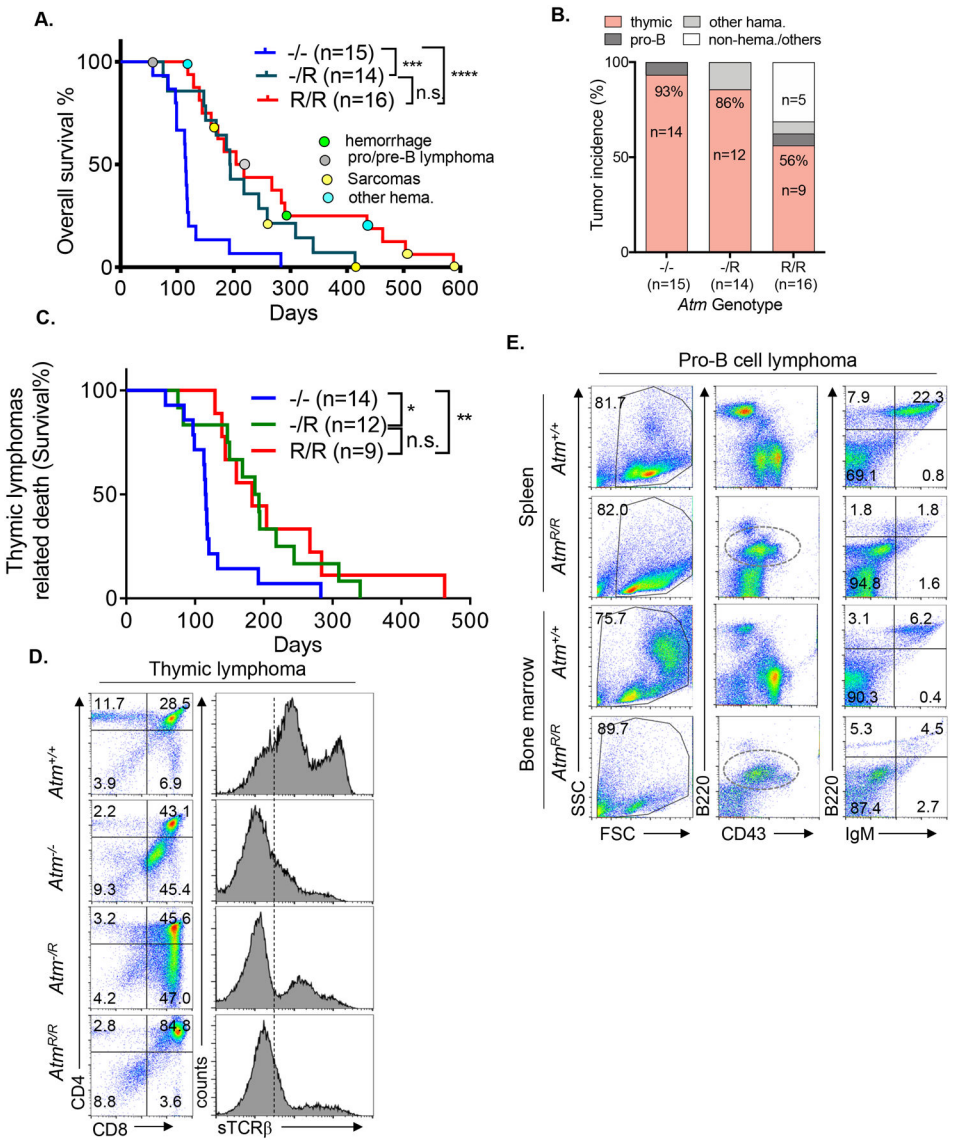

Fig 4. *Atm*$^{R/R}$ mice show delayed thymic lymphoma in comparison to Atm$^{-/-}$ mice.

A) Kaplan-Meier survival curve of *Atm*$^{-/-}$, *Atm*$^{-/R}$, and *Atm*$^{R/R}$ mice. The $t_{1/2}$ for total survival is 115 days for *Atm*$^{-/-}$, 194 days for *Atm*$^{-/R}$, and 211 days *Atm*$^{R/R}$ mice. The $\Delta t_{1/2}$ =96 days between *Atm*$^{-/-}$ and *Atm*$^{R/R}$ cohorts. Mantel-Cox/log-rank test was used for statistical analysis. The causes of death other than thymic lymphomas were marked on the graph with color-coded circles. Other hematological malignancies included a spectrum of CD43+B220+CD4−CD8− mess in the lymph nodes or other parts of the body. **B)** Incidence of detected tumors in analyzed *Atm*$^{-/-}$, *Atm*$^{-/R}$, and *Atm*$^{R/R}$ cohorts. The relative frequency of each category and the incidence (n) are marked. **C)** Kaplan-Meier survival curve of *Atm* $^{-/-}$, *Atm*$^{-/R}$, and *Atm*$^{R/R}$ mice that died of thymic lymphomas. The $t_{1/2}$ for thymic lymphoma is 115 days for *Atm*$^{-/-}$, 190 days for *Atm*$^{-/R}$, and 183 days *Atm*$^{R/R}$ mice. **D)** Representative FACS analysis of immature thymic lymphomas from *Atm*$^{-/-}$, *Atm*$^{-/R}$, and *Atm*$^{R/R}$ mice. **E)** Representative FACS analysis of pro-B cell lymphoma from an *Atm*$^{R/R}$ mouse. For **D)** and **E)**, flow cytometry analyses of a normal *Atm*$^{+/+}$ mouse is included as a control. For A and

C, Log-rank (Mantel-Cox) test was used to calculate the p-value. $p<0.01$, **; $p<0.001$, ***; $p<0.0001$, ****; n.s. $p>0.05$.

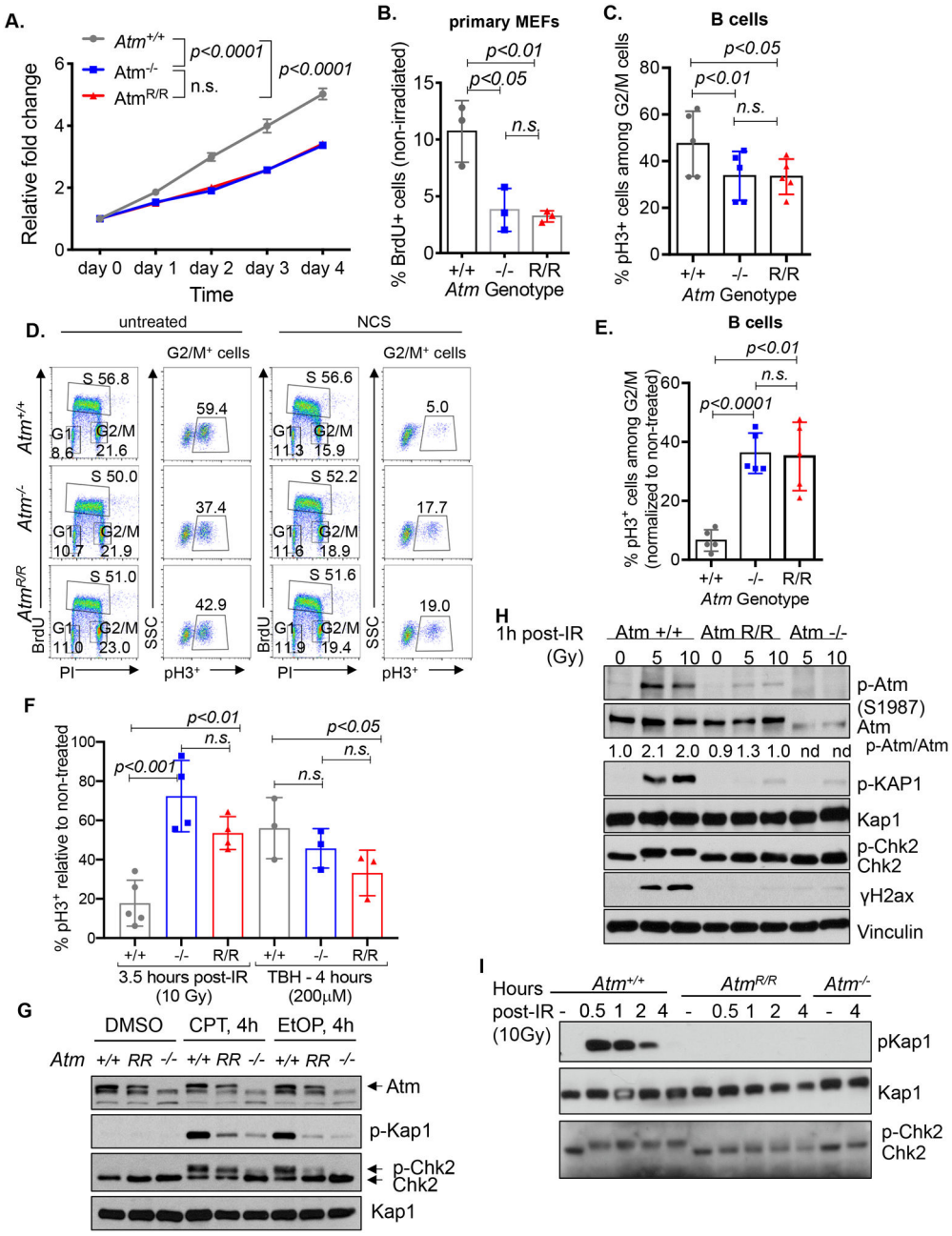

Fig 5. *Atm*$^{R/R}$ mice display cell cycle checkpoint defects.

A) Proliferation analysis of *Atm*$^{+/+}$, *Atm*$^{R/R}$, and *Atm*$^{-/-}$ primary MEFs. Data are presented as relative growth to the first measurement (marked as day zero). Measurements were done in at least three replicates per cell line. The error bars represent the standard deviation. ANOVA test p-value <0.0001 (****), p>0.05 (n.s., not significant). **B)** The percentage of BrdU^{+} *Atm*$^{+/+}$, *Atm*$^{R/R}$, or *Atm*$^{-/-}$ primary MEFs after a 30 min BrdU pulse. The bar graphs show mean ± standard deviation. P-values were calculated using unpaired two-tailed Student's *t*-test (n=3). **C)** The frequency of pH3+ cells from all G2/M (4N) cells in activated B cells (n=4 for each genotype). The bar graphs show mean ± standard deviation. The p-values were calculated using paired Student's t-test. **D)** Representative flow cytometry

analyses of the general cell cycle and the frequency of pH3+ cells with or without pulse damage by NCS (100 ng/mL for 1 hour). **E)** Bar graphs represent the percentages of pH3+ NCS treated cells relative to non-treated cells. The bar graphs show mean ± standard deviation. P-values were calculated using paired Student's t-test (n=4). **F)** G2/M cell cycle checkpoint analysis in primary MEFs 3.5 hours post-irradiation (10 Gy) or after 4 hours of TBH (200 μM) treatment. Mitotic cells were identified by positive pH3 staining. Bar graphs represent the percentages of pH3+ cells relative to non-treated conditions. The bars represent mean ± standard deviation. The p-values were calculated using paired Student's t-test (n>=3). **G)** Immunoblot analysis of $Atm^{+/+}$, $Atm^{R/R}$, and $Atm^{-/-}$ MEFs before or after treatment with CPT (0.2 μM) or EtOP (1 μM) for 4 hours. **H)** Immunoblot analysis of $Atm^{+/+}$, $Atm^{R/R}$, and $Atm^{-/-}$ MEFs 1 hour after irradiation with 5 Gy or 10 Gy dose. **I)** Immunoblot analysis of $Atm^{+/+}$, $Atm^{R/R}$, and $Atm^{-/-}$ MEFs at 0.5, 1, 2, and 4 hours after 10 Gy irradiation. For panel B. C, E, F, student's t-test is used, and $p>0.05$ = n.s. (not significant).

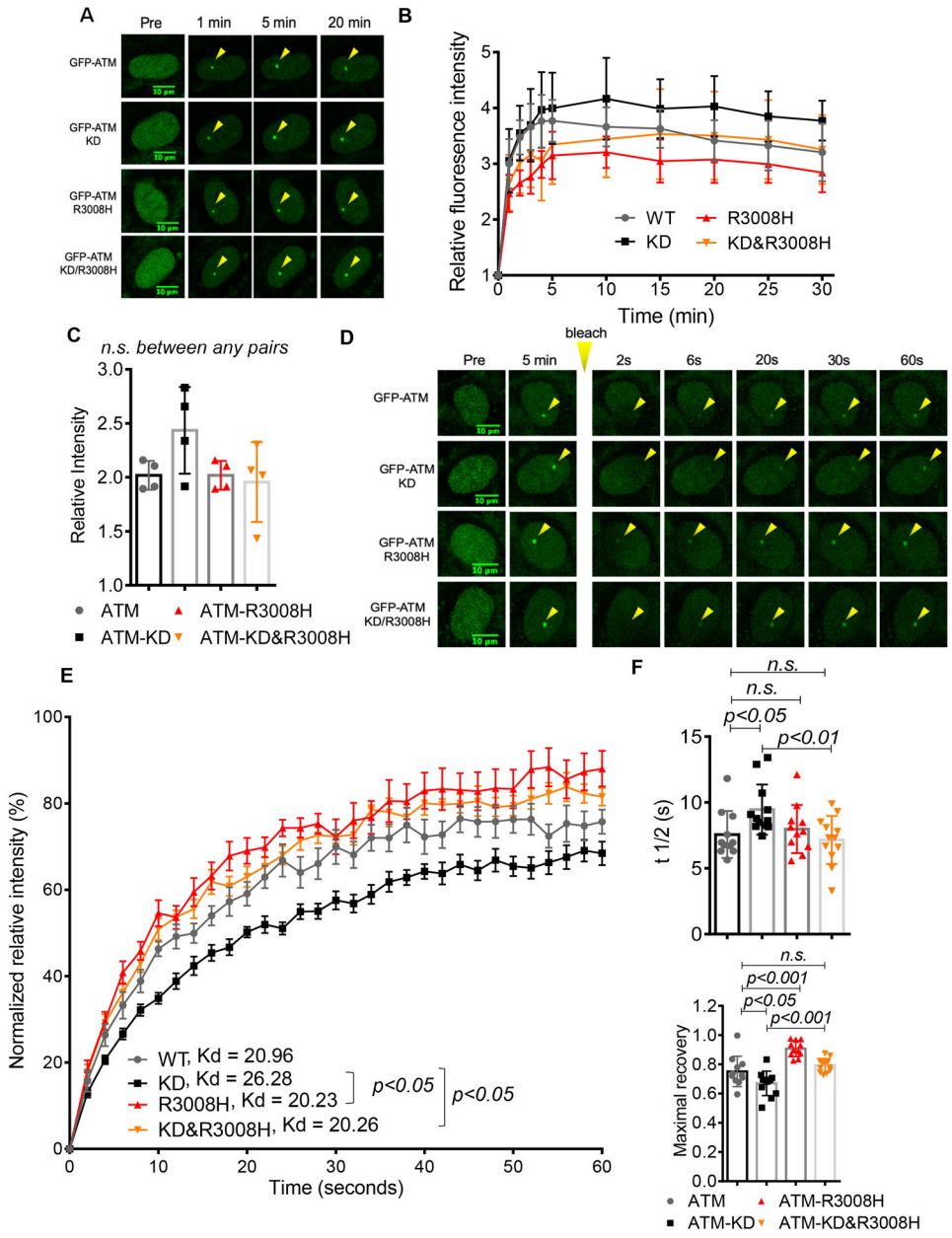

Fig 6. R3008H mutation rescues the exchange defects of the ATM-KD mutant.

Representative live-cell image analyses of GFP-ATM recruitment to micro-irradiation (405 nm) sites. Scale bar = 10 μm. The yellow arrowheads indicate the sites of damage. **B)** Relative fluorescence intensity of GFP-ATM variants accumulation at the DSBs sites over time. Each data point in the graph is the mean of relative ATM fluorescence measurements from each analyzed cell (n=4 per GFP-ATM variant). The error bars represent the standard deviation. **C)** Relative intensities of GFP-ATM variants at 5 min after micro-irradiation, plotted as mean ± standard deviation. Unpaired two-tailed Student's *t*-test was used for the statistical analysis. One of the two independent experiments is shown. **D)** and **E)** Representative FRAP images and analyses of GFP-ATM variants after photobleaching at 5 minutes after micro-irradiation. For **D)** scale bar = 10 μm. The yellow arrowheads point to

the site of micro-irradiation. For **E)** each data point depicted in the graph is the mean of normalized measurements (n>=11 per GFP-ATM variant). The error bars represent the standard error of the mean. The unpaired two-tailed student's *t*-test was used to calculate the p-values between the Kd. **F)** Bar graphs represent the mean ± standard deviation of $t_{1/2}$ (top) and the maximal recovery (bottom) for the indicated GFP-ATM variants. Unpaired two-tailed Student's *t*-test was used for the statistical analysis. For panel C and F, student's t-test is used, and p>0.05 = n.s. (not significant).